LANGMUIR

Article

pubs.acs.org/Langmuir

Role of Adsorption Phenomena in Cubic Tricalcium Aluminate Dissolution

Rupert J. Myers,*[,†,‡] Guoqing Geng,[†] Jiaqi Li,[†] Erich D. Rodríguez,[§,∥] Juyoung Ha,[⊥] Pinit Kidkhunthod,[▽] Garrison Sposito,[+] Laura N. Lammers,[+] Ana Paula Kirchheim,[§] and Paulo J. M. Monteiro[†]

[†]Department of Civil and Environmental Engineering, University of California, Berkeley, California United States

[‡]Yale School of Forestry & Environmental Studies, Yale University, 195 Prospect Street, New Haven, Connecticut 06511, United States

[§]NORIE/UFRGS - Building Innovation Research Unit, Department of Civil Engineering, Federal University of Rio Grande do Sul, Porto Alegre, Brazil

[∥]Polytechnic School of Civil Engineering, IMED, Passo Fundo, Brazil

[⊥]School of Environmental and Sustainability Sciences, Kean University, Union, New Jersey 07083, United States

[▽]Synchrotron Light Research Institute, 111 University Avenue, Muang District, Nakhon Ratchasima 30000, Thailand

[+]Department of Environmental Science, Policy, and Management, University of California, Berkeley, California 94720, United States

S *Supporting Information*

ABSTRACT: The workability of fresh Portland cement (PC) concrete critically depends on the reaction of the cubic tricalcium aluminate (C_3A) phase in Ca- and S-rich pH >12 aqueous solution, yet its rate-controlling mechanism is poorly understood. In this article, the role of adsorption phenomena in C_3A dissolution in aqueous Ca-, S-, and polynaphthalene sulfonate (PNS)-containing solutions is analyzed. The zeta potential and pH results are consistent with the isoelectric point of C_3A occurring at pH ∼12 and do not show an inversion of its electric double layer potential as a function of S or Ca concentration, and PNS adsorbs onto C_3A, reducing its zeta potential to negative values at pH >12. The S and Ca *K*-edge X-ray absorption spectroscopy (XAS) data obtained do not indicate the structural incorporation or specific adsorption of SO_4^{2-} on the partially dissolved C_3A solids analyzed. Together with supporting X-ray ptychography and scanning electron microscopy results, a model for C_3A dissolution inhibition in hydrated PC systems is proposed whereby the formation of an Al-rich leached layer and the complexation of Ca−S ion pairs onto this leached layer provide the key inhibiting effect(s). This model reconciles the results obtained here with the existing literature, including the inhibiting action of macromolecules such as PNS and polyphosphonic acids upon C_3A dissolution. Therefore, this article advances the understanding of the rate-controlling mechanism in hydrated C_3A and thus PC systems, which is important to better controlling the workability of fresh PC concrete.

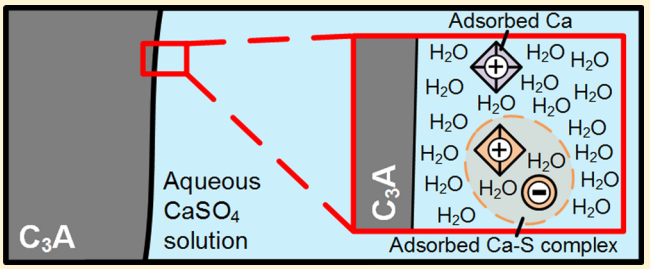

1. INTRODUCTION

Portland cement (PC) concrete is the second most used commodity after fresh water. Approximately ∼40 Gt of this material was produced in 2014 (assuming that PC concrete contains ∼10 wt % PC).[1] Most concrete is ready mixed at a concrete plant and then placed on site as a concentrated slurry,[1] which sets to form the ubiquitous material that constitutes most civil infrastructure in existence today and that will be built in the foreseeable future. Careful control of the PC concrete setting process is imperative to achieving a fluid, workable material throughout placement and to producing a strong and durable construction material. The rheology and setting time of fresh PC concrete are significantly controlled by adding solid $CaSO_4$ (typically gypsum, $CaSO_4{\cdot}2H_2O$) to retard the hydration of the highly reactive cubic tricalcium aluminate (C_3A, $Ca_3Al_2O_6$, where C is CaO and A is Al_2O_3) phase in PC, which can be prolonged for hours.

In PC, C_3A is generally present as intimately intermixed crystallites with other phases, which are mostly tri- and dicalcium silicate (Ca_3SiO_5 and Ca_2SiO_4, respectively) and tetracalcium aluminoferrite ($Ca_4Al_2Fe_2O_{10}$).[2] The structure of C_3A contains tetrahedral Al in $Al_6O_{18}^{18-}$ rings and Ca atoms in distorted octahedral or irregular bonding environments.[3−5] The dissolution of C_3A in portlandite ($Ca(OH)_2$)-saturated aqueous $CaSO_4$ solutions leads mainly to the precipitation of ettringite ($Ca_6Al_2S_3O_{18}{\cdot}32H_2O$) and alumino-ferrite-mono (AFm)

Received: September 21, 2016
Revised: November 29, 2016
Published: December 2, 2016

DOI: 10.1021/acs.langmuir.6b03474
Langmuir 2017, 33, 45−55

phases in CaO-Al_2O_3-SO_3-H_2O systems with mechanistically comparable yet slightly lower S/Al molar ratios (~0.1[6]) than that present in PC systems (~0.5[7]). AFm phases are layered double hydroxides based on substituted $Ca(OH)_2$-type structures. These AFm phases also precipitate initially in the absence of $CaSO_4$, although they are later destabilized to the more thermodynamically stable katoite ($Ca_3Al_2O_6{\cdot}6H_2O$) phase.[8] In the absence of $CaSO_4$, C_3A dissolution occurs so rapidly that most PC concrete irreversibly loses fluidity and prematurely flash sets, greatly reducing the workability and strength development.[2] Other compounds (admixtures) (e.g., $CaCl_2$,[9] organic admixtures, and polynaphthalene sulfonate (PNS)[10]) are also added to modify the reactivity of PC and the workability of fresh PC concrete, with their dosage depending on the reactivity of C_3A.[11] PNS is a synthetic commercial water-reducing admixture, typically polydispersed with a mean molecular mass of ≫1000 Da,[12,13] that adsorbs onto hydrated PC particles and retards C_3A dissolution.[11,13]

Despite the relatively low fraction of C_3A in PC (~5−10 wt %), the properties of fresh PC concrete in the induction period (i.e., the period of relatively high workability and low reaction rate of PC) critically depend on this phase. The C_3A/solution interface chemistry in aqueous $CaSO_4$ solutions and in water is significantly different,[14−16] with adsorption phenomena generally agreed to provide the key C_3A dissolution-inhibiting mechanism in the former system. The seminal work on this topic[14,17] used electron spectroscopy and Ar ion milling to identify an Al-rich leached layer at the C_3A/solution interface and electrophoresis and analytical chemistry methods to propose that both Ca ions and SO_4^{2-} complexes adsorb onto this layer and inhibit C_3A dissolution. This description is consistent with previous work[2,16] and is sustained by later research.[6,18,19] The cement research community has recently rallied in support of adsorbed SO_4^{2-} complexes providing the key C_3A dissolution rate controlling factor in aqueous $CaSO_4$ systems,[20,21] although not necessarily mentioning the Al-rich leached layer[14,17] to which these SO_4^{2-} complexes would adsorb onto.

The postulated complexation of Ca and SO_4^{2-} on partially hydrated C_3A is, however, based only on indirect macro- and/or microscopic evidence rather than direct molecular-scale information. Therefore, the chemistry and structure of the Al-rich leached layer and proposed Ca ions and SO_4^{2-} complexes are not known in enough detail to confirm the adsorption-controlled C_3A dissolution hypothesis. The proposed inhibiting effect of singly adsorbed SO_4^{2-} complexes on C_3A dissolution is also inconsistent with the adsorption behavior of SO_4^{2-} in metal (hydr)oxide systems, where it interacts as a weak to intermediate adsorbate, similarly to SeO_4^{2-}.[22] For example, the tendencies of SO_4^{2-} and SeO_4^{2-} to specifically adsorb onto (bayerite-type) $Al(OH)_3$, γ-Al_2O_3, δ-Al_2O_3, and goethite (α-FeOOH) decrease strongly with increasing pH,[23−26] with essentially no adsorption occurring above the pH of the point of zero charge (pH_{pzc}) (i.e., above pH 7−10). Therefore, the specific adsorption of SO_4^{2-} onto the partially dissolved C_3A surface at cement-relevant pH (i.e., pH >12) is unlikely because this surface is Al-rich and is chemically similar to Al (hydr)oxide.[14] Recent research has also identified the weak adsorption of Ca^{2+} on gibbsite ($Al(OH)_3$).[27] This finding contradicts the description of the partially dissolved C_3A surface provided by Skalny and Tadros,[17] who considered it to behave analogously to γ-Al_2O_3 and specifically adsorb Ca^{2+}.[28] A better understanding of the surface chemistry of partially dissolved C_3A in aqueous solutions relevant to fresh PC concrete (i.e., containing Ca and S and particularly at high pH) is needed to clarify these apparent contradictions. The effects of other commonly used admixtures (e.g., PNS) on the chemistry of the C_3A/solution interface chemistry are also incompletely understood.

Here, the surface chemistry of partially dissolved C_3A in various Ca- and S-containing aqueous solutions is analyzed by making use of the Gouy−Chapman−Stern model of the electric double layer (EDL).[29−31] The EDL is thus conceptualized to contain (i) an *s* plane related to the structural and proton charge at the solid surface; (ii) a Stern layer that contains *a* and β planes associated with inner-sphere and outer-sphere (i.e., separated by at least one water molecule) complexes, respectively; and (iii) a *d* plane further from the solid surface associated with the diffuse layer (diffuse ion swarm) that balances the surface charge. The adsorption of inner-sphere complexes is specific, whereas the adsorption of outer-sphere and diffuse layer complexes is nonspecific. The Debye length (κ^{-1}) is an intrinsic length scale of the EDL that is a measure of the distance from the charged particle surface from which co-ions (same charge as the particle surface) are excluded.[31] It is commonly associated with the plane of shear, which is assigned to the outer periphery of the Stern layer, including part of the diffuse layer.[30]

Zeta potential measurements of aqueous C_3A samples are obtained systematically as functions of the pH and solution chemistry here. This is important because so far only a limited set of conditions have been used to characterize the chemistry of the C_3A/solution interface.[14,15,32,33] S and Ca *K*-edge X-ray absorption spectroscopy (XAS) data are collected at the Synchrotron Light Research Institute (SLRI) and Brazilian Synchrotron Light Laboratory (LNLS), respectively. These data are analyzed to characterize unreacted and partially dissolved C_3A particles in gypsum-saturated solutions at the molecular level. This analysis represents a first attempt at simultaneously characterizing S and Ca *K*-edge XAS data of C_3A dissolution in aqueous $CaSO_4$ solutions, which is important to understanding and developing model molecular structures for S and Ca adsorbates on calcium aluminate hydrates. S and Ca *K*-edge XAS and zeta potential results are also obtained and discussed for key solid phases in the C_3A-$CaSO_4$-H_2O system, which have generally not yet been comprehensively analyzed.[15,33−35] Morphological information on partially dissolved C_3A particles is obtained by scanning electron microscopy (SEM) and complementary X-ray ptychographic imaging at the Advanced Light Source (ALS).[36] This article aims to unify these results to provide an advanced description of the surface chemistry of partially dissolved C_3A and insight into the rate-controlling mechanism of C_3A dissolution in PC-relevant aqueous solutions.

2. EXPERIMENTAL SECTION

2.1. Solids. The C_3A that was used (Mineral Research Processing Cie, hereafter MRP) was synthesized by firing a stoichiometric mixture of $CaCO_3$ and Al_2O_3 (both from Merck) twice at 1350 °C for 2 h in platinum vessels and ground to a fine powder in an intermediate step. Its particle size distribution (PSD) and specific surface area are shown in the Supporting Information (SI). The powder was lightly reground for ~30 s by hand in an N_2(g) atmosphere to create surface area that had been unexposed to air and then stored in vacuum-sealed bags before use. Scanning electron microscope (SEM) imaging (section 3.2) shows that particle diameters in the reground material are similar to the previously measured values. X-ray diffraction (XRD) and

DOI: 10.1021/acs.langmuir.6b03474
Langmuir 2017, 33, 45−55

Rietveld analyses (using PANalytical HighScore Plus) showed that the C_3A powder contained ≥99 wt % cubic C_3A (powder diffraction file (PDF) 01-070-0839) (estimated uncertainty = ±3 wt %). Free lime (CaO) was not identified in the X-ray diffractogram of the C_3A powder used (Figure S1, SI).

Reference zeta potential and XAS data were collected for several common phases in the C_3A-water(-calcium sulfate) system. These phases are ettringite (MRP), gypsum (Sigma-Aldrich), calcium aluminate ($CaAl_2O_4$, MRP), katoite (MRP), portlandite (Fisher Scientific), calcium hydroxyaluminate hydrate (OH-AFm, predominantly $Ca_4Al_2O_7{\cdot}13H_2O$), and calcium monosulfoaluminate hydrate (S-AFm, predominantly $Ca_4Al_2SO_{10}{\cdot}12H_2O$). The procedures used to synthesize OH-AFm and S-AFm are described in the SI. The thermogravimetric analysis (TGA) and XRD data collected for these precursor materials are shown in Appendix C (SI). These reference data were used to assist in analyzing the zeta potential, SEM, X-ray ptychography, and XAS results obtained for the C_3A-containing samples.

2.2. Zeta Potential and pH. Samples for zeta potential and pH analyses were synthesized under ambient laboratory conditions by hand-mixing 0.020 g of solids and 4.0 g of precursor solutions in polypropylene centrifuge tubes at a liquid/solid mass ratio (l/s) of ∼200 (i.e., a large stoichiometric excess of water was used). The pH values of the precursor solutions used were adjusted with 1 M NaOH (Fisher Scientific) or 1 M HCl (synthesized from 37.7 wt % HCl, J.T. Baker) before adding the solids, with an estimated ionic strength (I) range for these pH-adjusted solutions of $I < 0.3$ mol kg^{-1}. The aqueous solutions are water (18.2 × 10^6 Ω cm, produced using a Barnstead NANOpure II with a filter size of 0.2 μm), 0.013 M K_2SO_4 produced from K_2SO_4(s) (Sigma-Aldrich), 0.013 M $CaSO_4$ produced from $CaSO_4{\cdot}2H_2O$(s) (Sigma-Aldrich), 0.017 M $CaCl_2$ produced from $CaCl_2{\cdot}2H_2O$(s) (Fisher Scientific), and 0.03 wt % PNS (Mira 151, W. R. Grace & Co.—Conn.). This PNS solution contains S and Na concentrations of 2.3 × 10^{-3} and 3.8 × 10^{-3} mol L^{-1} (as determined by ICP-OES, with an estimated measurement error of ±10%), respectively. Its PNS content was set to achieve a (dry) polymer to C_3A mass ratio of 0.06. This ratio value was chosen to approximately represent the adsorption saturation of PNS in C_3A-containing K_2SO_4 systems for 30 min of hydration[13] (the solids fraction in bulk PNS was determined using ASTM C494), acknowledging that the amount of PNS required to attain saturation likely varies from one C_3A source to another.

An Accumet pH meter (Fisher Scientific), calibrated to standard pH 4, 7, and 10 (Fisher Scientific) and pH 13 (Ricca Chemical Company) buffer solutions at 24 ± 2 °C, was used to determine the pH of samples synthesized in this work (estimated absolute error = ±0.3). Measurements of the sample pH were obtained at the reaction times analyzed here (80, 130, 220, and 550 s). Electrophoretic mobility (u_E) data were obtained using a Zetasizer ZSP (Malvern Instruments, particle size range of 3.8 nm to 100 μm) and ZetaPALS (Brookhaven Instruments Corporation) instruments operated at 22.0 ± 0.2 °C. Two separate machines were used to improve the reliability of the results obtained. Zeta potentials (ζ) were calculated from the Smoluchowski equation (eq 1)

$$u_E = \frac{\varepsilon_0 \varepsilon \zeta}{\eta} \tag{1}$$

where ε_0 is the electric permittivity of free space (8.854 × 10^{-12} F m^{-1}) and ε and η are the relative permittivity and viscosity of the background electrolyte. (Values for water at 22 °C of ε = 79.6 and η = 0.9540 Pa s were used.) The Smoluchowski equation is valid for systems with $\kappa a \gtrsim 100$,[37] where a is the particle radius (Å) and κ^{-1} is the Debye length (Å) ($\kappa^{-1} = 2.8/I^{0.5}$ Å in the absence of organic compounds,[38] i.e., $\kappa^{-1} > 5.1$ Å here). This condition is attained here from the relatively large particle sizes of the solids used. Partial sedimentation of particles was identified in some samples during the electrophoresis experiments but was not corrected for.

Each zeta potential datum point reported here represents the mean value of 15 measurements taken during specified time intervals after C_3A and precursor solutions were mixed (i.e., 80 ± 20, 130 ± 30, 220 ± 60, and 550 ± 50 s). These reaction times were selected to sample the fastest times that the experiments could be reproducibly performed (limiting the precipitation of reaction products) and the effects of precipitation and the slight variation in l/s values used in the results. Measurements were repeated multiple times (section 3.1) to obtain an overall picture of the experimental uncertainty (estimated measurement error for each datum point is ±15 mV).

2.3. SEM and X-ray Ptychography. The same synthesis procedure used for the zeta potential and pH experiments was used to synthesize samples for the SEM and X-ray ptychography experiments (pH values modified to >12 by adding 1 M NaOH and mixing C_3A with precursor solutions at l/s ≈ 200), with the exception of the additional steps described below.

SEM samples were filtered after 80 s of mixing using 0.45 μm nylon filters and then washed with ≥99.9% ethanol (Koptec). The solids were then spread on carbon-tape-covered SEM sample holders and coated with carbon. The SEM experiment was performed immediately afterward using a Zeiss EVO Variable Vacuum Instrument -10 SEM operated at ∼0.001 Pa and in secondary electron mode at an extra-high tension voltage of 15.0 kV, a 50.0 μA beam current, a probe current of 14 pA, and a working distance of ∼12 mm. SEM images were additionally obtained on unreacted C_3A and C_3A reacted in 0.013 M $CaSO_4$ for 300 s. Samples prepared for soft X-ray ptychographic imaging at beamline 5.3.2.1 of the ALS were drop-cast onto 100-nm-thick Si_3N_4 windows (Norcada) without a filtration step. Excess liquid was quickly removed using Kimwipes (Kimtech). The samples were then immediately transferred to the instrument chamber and subsequently exposed to a 750 eV X-ray beam at ∼0.001 Pa. The pixel size of the reconstructed images obtained is ∼5 nm × 5 nm. Further details of the X-ray ptychography experimental setup used are presented in ref 36.

2.4. S *K*-edge XAS. S K-edge XAS was performed at beamline 5.2 (SUT-NANOTEC-SLRI) at the SLRI, Thailand, which operates at 1.2 GeV and 50−150 mA and produces 10^8−10^{10} photons s^{-1} at a bending magnet source. The beam has a lifetime of ∼12 h and an emittance of 41 nm rad. Experiments were conducted in fluorescence mode using a four-element Si drift detector (Vortex), an InSb(111) crystal monochromator, and a beam size of 20 mm × 1 mm. The XAS data collected were referenced by assigning 2472.0 eV to the lowest-energy inflection point of the K-edge absorption spectrum of S powder (oxidation state = 0, Sigma-Aldrich no. 414980). S K-edge X-ray absorption near-edge structure (XANES) and extended X-ray absorption fine structure (EXAFS) spectra were collected from 2402 to 3120 eV with step sizes of 5 eV up to 2452 eV, 0.2 eV from 2452 to 2502 eV, and 1−5 eV from 2502 to 3120 eV.

Reference solid phases (S-AFm, ettringite and gypsum) were mixed with ∼1 μm^3-sized 98 wt % BN (Sigma-Aldrich) at a respective mass ratio of 1:19, placed on a kapton tape backing, covered with polypropylene film, and then analyzed. Data for the 0.013 M $CaSO_4$ precursor solution was obtained in a cell with polypropylene film windows. Hydrated samples were synthesized by consecutively immersing C_3A, S-AFm, ettringite, or katoite in 0.013 M $CaSO_4$ at l/s ≈ 360 up to 300 s and then in two ≥99.9% ethanol (Koptec) solutions for 30 s, first at l/s ≈ 210 and then at l/s ≈ 140. These samples were then immediately transferred to a desiccator and vacuum-dried at 700 Pa over SiO_2 gel, pressed into smooth, thin (∼1 mm), flat disks once dry, and then stuck to a kapton tape backing and transferred to the He(g)-filled instrument chamber.

2.5. Ca *K*-edge XAS. Unreacted and partially reacted C_3A and gypsum were prepared for Ca K-edge XAS analysis by first spreading 0.020 g of C_3A or gypsum onto carbon-tape-covered sample stages. The partially reacted C_3A sample was produced by immersing a C_3A-covered sample stage into a 20 mL saturated gypsum solution for 1 s, which was then immediately rinsed with ≥99.9% ethanol (EMSURE, Merck) for 60 s to remove the excess aqueous solution. Samples were analyzed at the extended Ca K-edge (3960−4800 eV). Experiments were performed at beamline SXS, LNLS, located at the 4° port of bending magnet station D004A using a double-crystal Si(111) monochromator, a photon flux of 2.4 × 10^{10} photons s^{-1} at 3 keV

DOI: 10.1021/acs.langmuir.6b03474
Langmuir 2017, 33, 45−55

machine energy, and a current of 100 mA. Spectra were collected in total electron yield (TEY) mode at 2×10^{-4} Pa. Three to ten spectra were collected and averaged for each sample. Energy calibration was performed using the L_3 $2p_{3/2}$ Mo peak by assigning the energy of the first edge inflection point to 2520 eV. The S and Ca *K*-edge XAS data were analyzed using the Athena and Artemis modules of the Demeter v.0.9.24 software,[39] which utilizes FEFF6 and IFEFFIT v.1.2.12.

3. RESULTS AND DISCUSSION

3.1. Zeta Potential, pH, and ICP-OES. The following coupled zeta potential and solution chemistry analysis is used to investigate the influence of cations (e.g., Ca^{2+} and $CaOH^+$), anions (e.g., SO_4^{2-} and Cl^-), and ion pairing (e.g., $CaSO_4^0$) on the surface potential of C_3A and chemistry at the C_3A/solution interface. Zeta potential values measured at different reaction times are similar at constant pH for each reaction system. The data obtained for C_3A immersed in water are consistent with an isoelectric point (IEP) at pH ~12 and the existing data for this phase,[14] with the zeta potential decreasing from ~40 mV below pH ~10 to −30 mV at pH 12.8 (Figure 1A). The large range of zeta potentials measured for C_3A at pH >12 here may result from heterogeneous C_3A dissolution and thus a variety of chemistries at the C_3A surface and the presence of surface-bound reaction products (section 3.2).

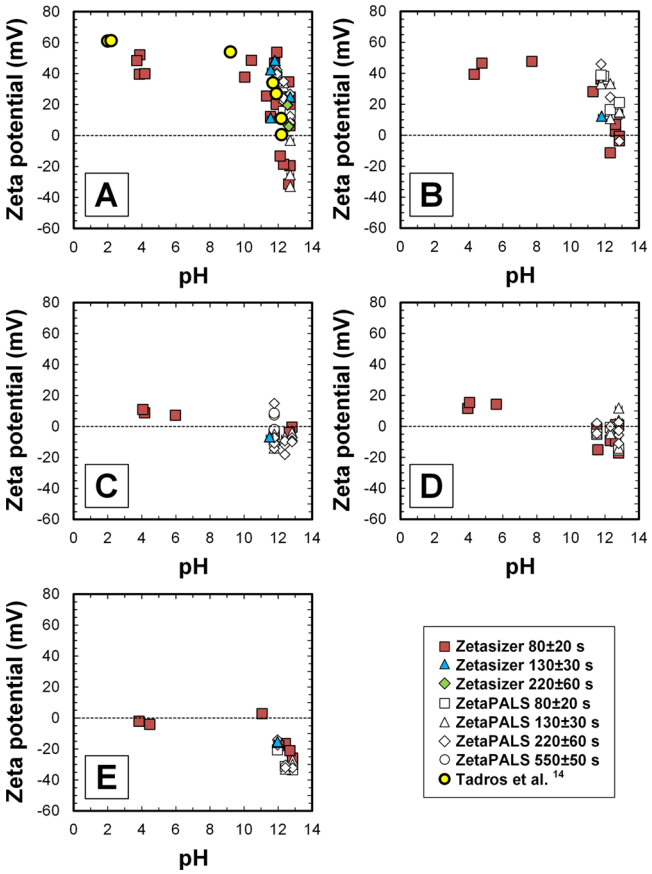

Figure 1. Zeta potentials of C_3A in (A) water, (B) 0.017 M $CaCl_2$, (C) 0.013 M K_2SO_4, (D) 0.013 M $CaSO_4$, and (E) 0.03 wt % PNS as functions of pH and time after mixing (80 ± 20 to 550 ± 50 s). The dashed horizontal lines are intended as eye guides only. The estimated uncertainties in the pH and zeta potential values are indicated by the size of the symbols used and the spread of the data points, respectively. Data from ref 14 are for C_3A reacted in water (l/s = 250) for 2 min with the pH adjusted by aqueous HCl or NaOH solutions. The instruments used to produce each datum point are indicated in the legend. Plots of the pH >10 regions in A–E are shown in the SI.

Significantly increased zeta potentials for C_3A in 0.017 M $CaCl_2$ relative to water are measured only at pH > 12 (Figure 1B) and are mostly non-negative in this pH range. The similar yet less-negative zeta potentials measured for C_3A in 0.017 M $CaCl_2$ relative to water suggests that the EDL is compressed in the former system relative to the latter because of its increased ionic strength. The data do not show an inversion of the zeta potential at pH >12 with respect to these systems, which does not support the assignment of specifically adsorbed Ca on partially dissolved C_3A.

The zeta potentials measured for C_3A in 0.013 M K_2SO_4 are close to zero over the range of pH values analyzed (Figure 1C) and are within the range of zeta potentials measured for C_3A in water at pH ≥11.5. The IEP of C_3A is identified to occur at pH ~12 in this system. The overall range of zeta potential values for C_3A immersed in 0.013 M K_2SO_4 is greatly reduced relative to that for the 0.017 M $CaCl_2$ system, indicating that SO_4^{2-} ions are much more effective at compressing the diffuse layer than Cl^- ions because of their increased effect on ionic strength. It is expected that SO_4^{2-} is the dominant aqueous S species here because K_2SO_4 is a strong electrolyte and $pK_{a2}(H_2SO_4) \approx 2$. Charge reversal is not identified in the 0.013 M K_2SO_4 system relative to water, which can suggest that SO_4^{2-} is nonspecifically adsorbed at pH <12, although it is not possible to unambiguously determine the molecular structure of adsorbed SO_4^{2-} complexes from these zeta potential data alone. However, the specific adsorption of SO_4^{2-} onto C_3A is not supported by existing work: adsorbed inner-sphere SO_4^{2-} would be consistent with C_3A dissolution inhibition by blocking surface sites from reacting with aqueous species, although only small differences in the rates of heat released and solid phases produced by C_3A dissolution in water, Na_2SO_4 and K_2SO_4, are measured. (Additional details regarding ref 40 are provided as SI.[13,40])

Similar results are obtained for C_3A in 0.013 M K_2SO_4 and 0.013 M $CaSO_4$ (Figure 1C,D). The IEP of C_3A is identified to occur at pH ~12 in the latter system. The significantly reduced range of zeta potentials measured for C_3A in 0.013 M $CaSO_4$ relative to that for 0.017 M $CaCl_2$ is again consistent with SO_4^{2-} more effectively compressing the diffuse layer of C_3A than Cl^- and shows that this effect, assigned to ionic strength differences, is essentially independent of the balancing cation (Ca^{2+} or K^+). The absence of a reversal in zeta potential values at constant pH in this 0.013 M $CaSO_4$ system relative to water is consistent with assigning Ca complexes (e.g., Ca^{2+} and $CaOH^+$) and SO_4^{2-} to nonspecifically adsorbed species in the aqueous C_3A systems analyzed here.

On the basis of current and prior observations of zeta potentials in aqueous C_3A systems,[14,15,32,33] it is not possible to conclude that Ca or S alone inhibits C_3A dissolution through an adsorption mechanism. However, the significance of Ca in inhibiting C_3A dissolution is supported by reported reduced C_3A dissolution rates in the presence of aqueous solutions with higher Ca concentrations (e.g., aqueous $CaSO_4$[6,17] and $CaCl_2$ solutions[41]) and also by reported uninhibited C_3A dissolution rates in aqueous Na_2SO_4 solutions (lower Ca concentration).[40] Given the consensus that $CaSO_4$ significantly affects C_3A dissolution rates, a cooperative effect can be proposed to arise whereby Ca and S together act to inhibit C_3A dissolution, with this effect being strongest in the presence of both elements. This effect could be manifest through the adsorption of the

DOI: 10.1021/acs.langmuir.6b03474
Langmuir 2017, 33, 45–55

Ca−S ion pair complexes (e.g., $CaSO_4^0$, which occurs in 12 < pH < 13 aqueous $CaSO_4$ solutions at significant nonzero concentrations that would not be lowered by adsorption because of continuous replenishment through rapid ion-pair formation in solution) onto the Al-rich leached layer to maintain a high concentration of Ca at the C_3A/solution interface, decreasing the local undersaturation of the aqueous solution with respect to C_3A. This effect would not require the presence of specifically adsorbed complexes. The Ca−S ion pair complexes may be viewed as an intermediate step in the nucleation and growth of surface-bound solid hydration products (e.g., AFm and ettringite)[42] because of their close proximity to the C_3A surface, which could additionally inhibit C_3A dissolution through enhanced surface polymerization and blocking of reactive surface sites (section 3.5).[30] Surface-bound precipitates and adsorbed Ca−S ion pair complexes are explored further below. This analysis does not preclude differences in adsorption behavior with respect to different surface site types (e.g., step, kink, and adatom[43]).

This pH and zeta potential analysis is also applied to aqueous PNS systems to better understand the adsorption behavior of PNS on C_3A because it is a commonly used admixture. Analogous to the 0.013 M K_2SO_4 and 0.013 M $CaSO_4$ systems, the zeta potentials of C_3A are reduced to approximately zero in 0.03 wt % PNS at pH <11.5 (Figure 1E). However, the zeta potentials of C_3A in 0.03 wt % PNS at pH >11.5 are all negative; therefore, PNS has inverted the zeta potential of C_3A in this system relative to the positive values obtained in water in this pH range. This result indicates that PNS adsorbs onto partially dissolved C_3A. This interpretation is consistent with the reported C_3A dissolution-inhibiting action of PNS[13,32] because the adsorption of macromolecules such as PNS would facilitate the blocking of reactive surface sites. The zeta potential results would then suggest that the adsorption of PNS onto solid reaction products is also likely, particularly onto phases such as ettringite[34] and AFm[44] that specifically complex SO_4^{2-} (the latter of which precipitates here, see section 3.2), because the chemistry of SO_4^{2-} and $-SO_3^-$ functional groups in PNS is similar.[45] Existing research shows that PNS alters the chemistry and morphology of ettringite,[33,46] consistent with this interpretation. The influence of surface-bound precipitates is explored further below.

3.2. SEM and X-ray Ptychography. X-ray ptychographic and SEM images of partially dissolved C_3A particles were obtained to qualitatively assess the influence of surface-bound precipitates on the zeta potential and pH data and to compare with the S and Ca *K*-edge XAS results (sections 3.3 and 3.4). Solid reaction products with predominantly hexagonal plate-type morphology, most likely AFm phases,[9,40] are observed to precipitate directly on C_3A particles (red arrows) reacted for 80 s in NaOH-modified (pH 12.5−13) water (Figure 2B) and 0.017 M $CaCl_2$ (Figure 2C), 0.013 M K_2SO_4 (Figure 2D), 0.03 wt % PNS (Figure 2E), and 0.013 M $CaSO_4$ (Figure 2F) by SEM (main plot areas) and X-ray ptychography (insets). Hexagonal platelets are also identified on C_3A particles reacted in 0.13 M $CaSO_4$ for 300 s (Figure 2G). Needle-shaped precipitates are not observed, showing that ettringite has not formed to a major extent in any of the S-containing samples. This result is consistent with the literature for C_3A hydrated in aqueous $CaSO_4$[6,8,40,47] and Na_2SO_4[40] solutions at these reactions times (typical bulk molar S/Al ratios = 0.1−0.5), where the precipitation of the AFm phases dominates.

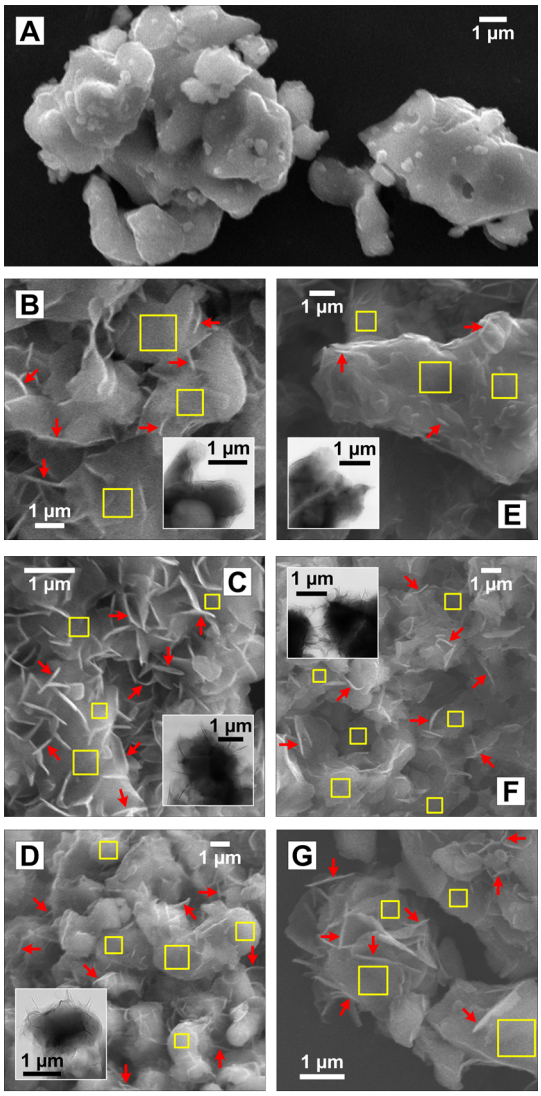

Figure 2. SEM (main plot areas) and X-ray ptychographic (insets) images of (A) unreacted C_3A, C_3A reacted in (B) water, (C) 0.017 M $CaCl_2$, (D) 0.013 M K_2SO_4, (E) 0.03 wt % PNS, and (F) 0.013 M $CaSO_4$ for 80 s with pH values of the precursor solutions adjusted to 12.5−13 using 1 M NaOH, and (G) C_3A reacted in 0.013 M $CaSO_4$ for 300 s. In B−G, precipitates with hexagonal platelet-type morphologies are marked by red arrows and the exposed C_3A surface area is marked by unfilled yellow squares.

Moderate to high proportions of the partially dissolved C_3A surface are exposed in the reacted samples (Figure 2B−G, unfilled yellow squares). The exposed surface area is qualitatively assigned to visually smooth areas with no hexagonal plate-shaped features that are characteristic of solid reaction products. This interpretation is consistent with the visually smooth surfaces of the unreacted C_3A particles imaged by SEM (Figure 2A). The exposed C_3A surface area is irregularly spaced in each reacted sample. Moderate amounts of both solid reaction products and exposed C_3A surface area are observed in the images of C_3A partially reacted in water, 0.017 M $CaCl_2$, 0.013 K_2SO_4, and 0.013 M $CaSO_4$. Fewer precipitates are identified on C_3A particles partially reacted in 0.03 wt % PNS, thus PNS has inhibited the dissolution of C_3A in this system. In summary, the SEM and X-ray ptychography results show that precipitates cover low (Figure 2D) to moderate (Figures 2B,C,E,F) proportions of the partially dissolved C_3A

DOI: 10.1021/acs.langmuir.6b03474
Langmuir 2017, 33, 45−55

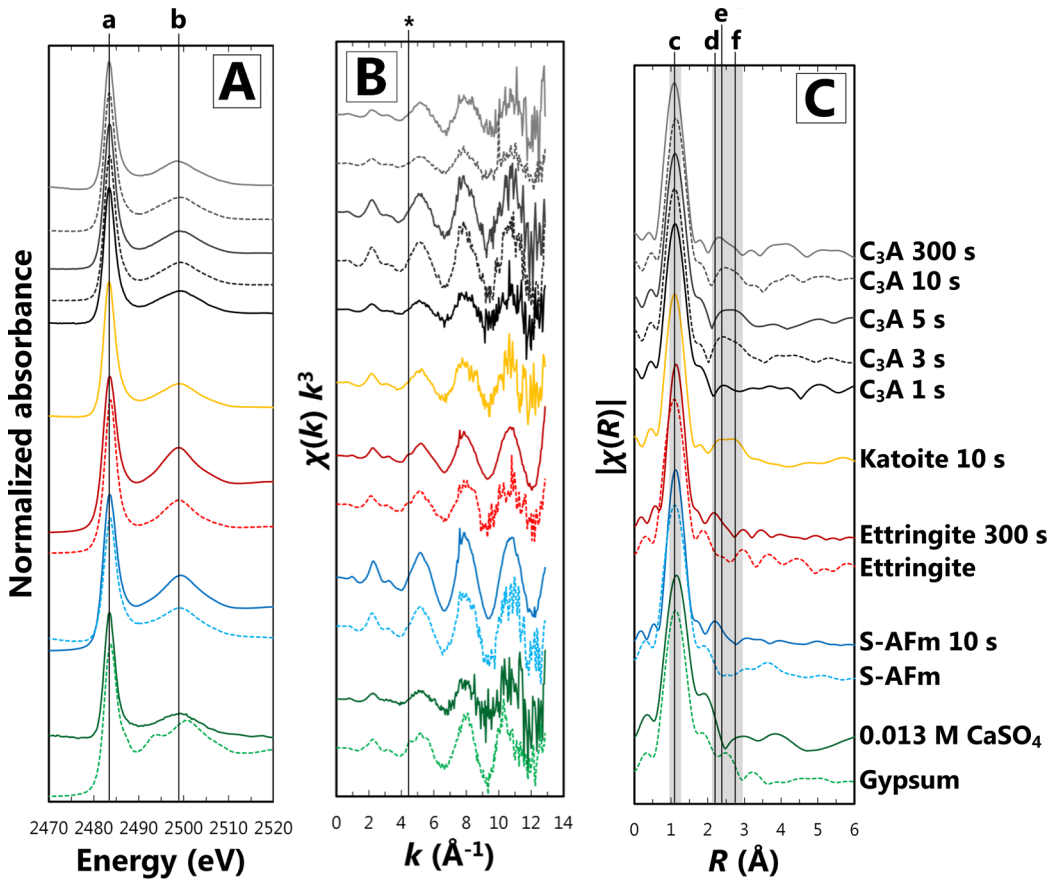

Figure 3. Normalized S *K*-edge XAS results for reference phases and C_3A systems, with times (in seconds, abbreviated as s) denoting the durations that the specified materials were immersed in 0.013 M $CaSO_4$ prior to analysis (pH during immersion ∼11−12): (A) S *K*-edge XANES spectra; (B) k^3-weighted χ data; and (C) magnitudes of the RSFs (radial structure functions) of the Fourier-transformed χ data. Characteristic features are marked by labeled vertical gray shaded regions and lines (discussed in the text).

surface. Therefore, the SEM and X-ray ptychography results signify that surface-bound precipitates have secondary rather than dominant effects on the zeta potential values and trends shown in Figure 1.

3.3. S *K*-edge XAS. S *K*-edge XAS data were obtained to directly analyze the chemistry of S adsorbed on C_3A partially reacted in 0.013 M $CaSO_4$. The S *K*-edge XANES spectra (Figure 3A) are all characteristic of S in the 6+ oxidation state (i.e., SO_4^{2-}), with peak *a* located at 2483.5−2483.8 eV,[48] which represents the transition of the 1s core electron to the 3p-like t_2 state.[48] With the exception of gypsum, all of the spectra show a broad peak *b* at 2499 eV that is assigned to multiple scattering (MS) resonances.[48] The S *K*-edge XANES spectrum for gypsum contains three distinct post-edge peaks, consistent with existing results.[48,49] These peaks are also reported for anhydrite.[50] The features of the ettringite and S-AFm spectra are consistent with the published S *K*-edge XANES data for these phases.[48−50]

The S *K*-edge XANES spectra for C_3A and katoite immersed in 0.013 M $CaSO_4$ (Figure 3A) represent SO_4^{2-} in S-containing reaction products and/or residual (formerly aqueous or adsorbed) SO_4^{2-} remaining after washing with ethanol and drying. The significant differences between these XANES spectra and those obtained for gypsum show that gypsum is absent in the katoite- and C_3A-containing samples. This analysis is supported by the k^3-weighted χ data (Figure 3B) collected for these samples, in which the spectrum for gypsum contains a shoulder at 4.5 $Å^{-1}$ (peak *) but the spectra for the C_3A- and katoite-containing samples do not. A shoulder at this *k* value is also present in the k^3-weighted χ data for ettringite (peak *, Figure 3B), both dry and after immersion in 0.013 M $CaSO_4$ for 300 s, ruling out the presence of this phase in the C_3A- and katoite-containing samples. This result is consistent with the absence of ettringite (needle-like precipitates) in the SEM images at this reaction time (Figure 2G, section 3.2). The k^3-weighted χ data for the katoite and C_3A samples, 0.013 M $CaSO_4$, and for the systems containing S-AFm, are qualitatively similar.

The magnitudes of the radial structure functions (RSFs) obtained by Fourier transforming the χ data (Figure 3C), which represent approximate interatomic correlations between S and nearby atoms in real space (modified slightly negatively from the true interatomic correlations by the phase function[51]), all show a dominant peak at ∼1.1 Å (peak *c*) that is assigned to the single scattering (SS) of S−O atoms in SO_4^{2-} tetrahedra. The minor peaks at smaller distances are artifacts caused by truncating the Fourier transform and do not correspond to scattering atoms. The position of this peak corresponds to true atomic S−O distances of ∼1.3−1.5 Å in ettringite,[52] S-AFm,[53] and gypsum.[54] The RSF curves for ettringite and S-AFm immersed in 0.013 M $CaSO_4$ show a secondary peak at 2.2 Å (peak *d*) that is enhanced relative to the spectra obtained for these materials when measured without immersion in 0.013 M $CaSO_4$. This peak likely corresponds to MS of S−O−O atoms, which is predicted from FEFF path-length calculations via Artemis software[39] using the bulk crystal structures of these

DOI: 10.1021/acs.langmuir.6b03474
Langmuir 2017, 33, 45−55

materials.[52,53] The RSF curve for gypsum shows a peak at 3.2 Å that can be assigned to SS of non-neighboring S−O atom pairs positioned relatively closely to SO_4^{2-} tetrahedra. The S−O MS peak at 2.2 Å that is expected for gypsum (from FEFF calculations[39] using its bulk crystal structure) is not apparent in the RSF data, potentially hidden behind the high-angstrom contributions from single-scattering S−O atoms in SO_4^{2-} tetrahedra at this *R* distance.

The spectra for the C_3A samples show a broad secondary peak composed of two resonances at ∼2.4 Å (peak *e*) and ∼2.7 Å (peak *f*). The slightly modified shape and position of this peak in the RSF curve for C_3A immersed in 0.013 M $CaSO_4$ for 300 s to lower *R* distances at ∼2.3 Å (i.e., toward peak *d*, Figure 3C) are assigned to the increased number of S-AFm precipitates at this reaction time relative to 1−10 s. This assignment is consistent with the hexagonal plate-like precipitates observed by SEM after immersion in 0.013 M $CaSO_4$ for 300 s (Figure 2G) and as ettringite, which is the only other material that contains this peak here, was previously discounted on the basis of the k^3-weighed χ data (Figure 3B). This analysis does not preclude the possibility that the hexagonal plate-like precipitates are partially AFm intercalated with other anions (e.g., OH^-).

The broad secondary peak (peaks *e* and *f*) in the S *K*-edge XAS spectra for the C_3A samples is also present in the RSF for katoite immersed in 0.013 M $CaSO_4$ for 10 s but not in the spectra for any other sample. The zeta potential and pH data obtained here for katoite are similar in water, −18.7 mV at pH 12.5, and in 0.013 M K_2SO_4, −17.2 mV at pH 12.4, consistent with a datum reported elsewhere.[35] Therefore, these data do not show a significant correlation between the EDL potential of katoite and the aqueous SO_4^{2-} concentration or ionic strength. A recent electron microprobe analysis found no evidence for significant S incorporation into Si hydrogarnet (katoite is the Si-free end member of the hydrogarnet solid solution). The results of that work also indicate that the dissolution extent of katoite would be very low under the experimental conditions employed here (i.e., immersed in 0.013 M $CaSO_4$ for 10 s at room temperature).[55] Therefore, these results most likely indicate that the SO_4^{2-} in the RSF of the katoite system is not structurally incorporated into the solid phase or specifically adsorbed but is rather adsorbed in the outer-sphere, diffuse layer, or residual aquo SO_4^{2-} from the bulk solution that has deposited on the particle surface during sample preparation (washed with ethanol and subsequently dried). Consequently, the broad secondary resonance containing peaks *e* and *f* in the C_3A samples can be assigned to these same deposited SO_4^{2-} complexes. A more detailed analysis comparing well-established model molecular structures of SO_4^{2-} adsorbates on calcium aluminate hydrate phases with these S EXAFS spectra and a better understanding of the molecular structure of the partially dissolved C_3A surface are necessary to confirm the identity of these S-bearing complexes: this work presents a first step toward this goal.

3.4. Ca *K*-edge XAS. Surface-sensitive Ca *K*-edge XAS data (the typical TEY sampling depth is a few nanometers) were obtained to assess the chemistry of Ca at the C_3A/solution interface on initial dissolution in aqueous $CaSO_4$ solution (saturated with respect to gypsum, ∼0.017 M $CaSO_4$). The Ca *K*-edge XANES spectra for gypsum, C_3A, and C_3A reacted in this solution for 1 s are similar (Figure 4A). Each spectrum contains a major peak *b* at ∼4055.5 eV corresponding to the 1s → 4p transition,[56] minor peaks *c* (4056 eV), *d* (4064.5 eV), *e* (4075 eV), and *f* caused by MS, and peak *c* that corresponds to the 1s → 5s transition.[56] Peak *f* occurs at a lower energy in the XANES spectrum for gypsum (4083 eV) relative to that for the C_3A samples (∼4090 eV). The additional shoulders (peak *a*) at 4033.3 eV in the spectra for the C_3A samples are ∼1 eV lower relative to its position in the spectrum for gypsum (at 4034.3 eV), which is consistent with the lower average coordination number of Ca atoms in C_3A (7.3) relative to 8 in gypsum[5] because the Ca *K*-edge energy generally increases as a function of the coordination number.[57] The minor resonances in the gypsum Ca *K*-edge XANES spectrum are less intense relative to those previously reported,[58] although they occur at the same energies. The lack of a double peak at peak *b* in the spectra for the sample containing C_3A reacted in saturated gypsum solution for 1 s, characteristic of ettringite,[58] indicates that this phase is not present in this system, which is consistent with the S *K*-edge XAS results and analysis presented in section 3.3.

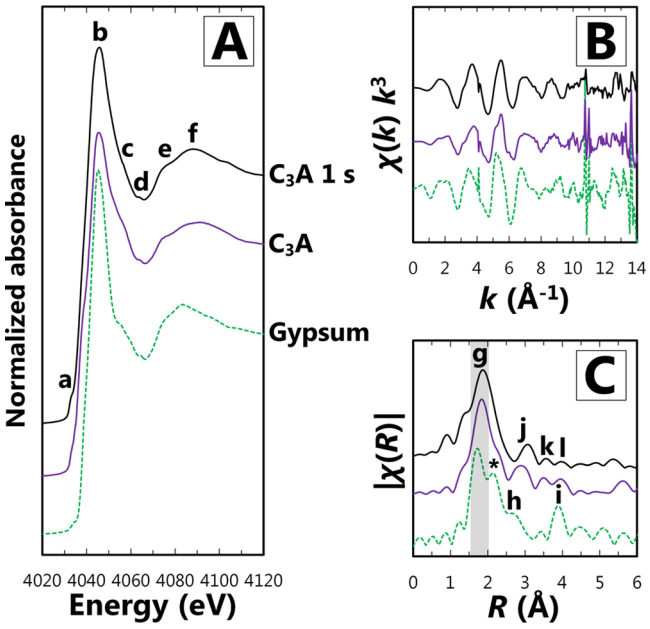

Figure 4. Normalized Ca *K*-edge XAS results. (A) Ca *K*-edge XANES spectra; (B) k^3-weighted χ data; and (C) magnitudes of the RSFs of the Fourier transformed χ data. C_3A immersed in a gypsum-saturated solution (∼0.017 M $CaSO_4$) prior to analysis (pH during immersion ∼11−11.5) for 1 s (abbreviated as s) is marked as C_3A 1 s (black solid lines), and data for gypsum and C_3A are represented by dashed green and solid purple lines, respectively. In C, the *g* peaks are marked by the gray shaded region.

The k^3-weighted χ data for C_3A and C_3A reacted in saturated gypsum solution for 1 s are similar (Figure 4B), differing substantially from the data collected for gypsum. All of the data have relatively poor signal-to-noise ratios at $k \gtrsim 10$ Å^{-1} and anomalous spikes in intensity at 4.1 Å. The RSF for gypsum (Figure 4C) is generally consistent with both FEFF calculations[39] using its known crystal structure[54] and previously reported Ca EXAFS data for this phase,[58] which contains the major Ca−O SS peak g (1.7 Å) and additional peaks *h* (2.7 Å) and *i* (3.9 Å) that correspond to SS of Ca−S[58] (Ca coordinated with O atoms in SO_4^{2-} groups[54]) and Ca−Ca atoms, respectively. Peak * is anomalous because it is not present in the previously reported RSF[58] and does not correspond to any strong resonances determined through the FEFF calculations.

The RSF for gypsum differs greatly from the RSFs for the C_3A samples (Figure 4C). The positions of the features in the

DOI: 10.1021/acs.langmuir.6b03474
Langmuir 2017, 33, 45−55

RSFs for the C_3A samples (Figure 4C) are consistent with FEFF calculations of Ca scattering paths in bulk C_3A:[4] major Ca−O SS peak *g* occurs at an *R* distance of ∼1.9 Å; peak *j* (2.9−3.1 Å) corresponds to SS of Ca−Ca and Ca−Al atoms; peak *k* (∼3.5 Å) represents SS of Ca−Al, Ca−O, and Ca−Ca atoms and MS of Ca−O−Al and Ca−O−Al−O atoms; and peak *l* (4 Å) corresponds to SS of Ca−O atoms. However, the location of peak *j* is shifted by 0.2 Å to a higher *R* value in the spectrum for C_3A immersed in 0.013 M $CaSO_4$ for 1 s relative to unreacted C_3A (3.1 and 2.9 Å, respectively, Figure 4C). This result shows that the initial reaction of C_3A in saturated gypsum solution has significantly modified the atomic configurations of Ca atoms that are next-nearest neighbors to Ca and Al atoms in C_3A. The specific adsorption of Ca onto the Al-rich leached layer of partially dissolved C_3A (i.e., through Ca−O−Al bonding) would result in distances between next-nearest neighboring Ca and Al atoms of ∼3 Å and so can be consistent with this result, although this assignment cannot be made because of the preliminary nature of the analysis presented here. Additional work (e.g., molecular simulations[34]) and/or an extension of this Ca EXAFS analysis through the use of model adsorbate molecular structures and a better understanding of the chemistry of partially dissolved C_3A is necessary to better determine the cause of this difference.

3.5. Model of C_3A Dissolution Inhibition in Aqueous Solutions. The results presented in sections 3.1−3.4 do not identify SO_4^{2-} or Ca cations as EDL potential-determining complexes and so do not indicate that they specifically adsorb to the Al-rich leached layer at the partially dissolved C_3A surface. This adsorption behavior is consistent with neither SO_4^{2-} nor Ca cations alone providing the key rate-controlling mechanism for C_3A dissolution in PC-relevant aqueous solutions (i.e., with pH > 12 and relatively high S and Ca concentrations ($\gtrsim$10 mmol L^{-1})). A more complex mechanism and potentially involving more than one chemical constituent would then be needed, considering that C_3A dissolution is uninhibited in Na_2SO_4(aq),[40] overall inhibited[41] although more precipitates are initially formed in $CaCl_2$(aq) (i.e., within the first few minutes of hydration[9]), and inhibited in $CaSO_4$(aq).[6]

Those previously reported results[6,40] show that C_3A dissolution becomes increasingly inhibited as a direct function of the aqueous Ca concentration in S-containing aqueous solutions. There is also a prevailing general consensus that S plays a key C_3A dissolution rate-controlling role in PC-relevant aqueous solutions.[20,21] This understanding can be reconciled with the results shown here if the presence of soluble S increases the local concentration of Ca at the C_3A/solution interface, thereby acting to decrease the dissolution rate of Ca in the Al-rich leached layer that forms through the dissolution of C_3A (and consequently inhibits the dissolution of the underlying C_3A solid, Figure 5).[17,59] Nonspecific adsorption of Ca−S ion pair complexes (section 3.1) onto this leached layer is consistent with this explanation and with the results presented here.

Solutions relatively rich in Ca and S are produced through the initial hydration of C_3A and PC in the presence of $CaSO_4$. Ca concentrations of 20−40 and 10−25 mmol L^{-1}, S concentrations of 10−20 and 50−200 mmol L^{-1}, and pH values of ∼12.5 and ∼13 are measured for $CaSO_4$-containing aqueous C_3A and PC systems before complete dissolution of the solid $CaSO_4$ source, respectively.[6,7,60] If the adsorption of Ca−S complexes controls the dissolution rate of C_3A in aqueous $CaSO_4$ solutions, then these adsorbates will accumulate at the partially dissolved C_3A surface during this initial reaction period. Net desorption or consumption of adsorbed Ca−S complexes would occur if the bulk solution becomes and remains sufficiently depleted in Ca and/or S. The local undersaturation with respect to C_3A surface sites and the C_3A dissolution rate would then consequently increase and remain elevated; otherwise, a net accumulation of Ca−S complexes at the C_3A/solution interface recurs (to again inhibit C_3A dissolution). This scenario is consistent with the reported rapid reaction of C_3A in PC-relevant systems once the solid $CaSO_4$ source completely dissolves (i.e., when the bulk aqueous Ca and S concentrations decrease rapidly in fresh hydrated PC[7]

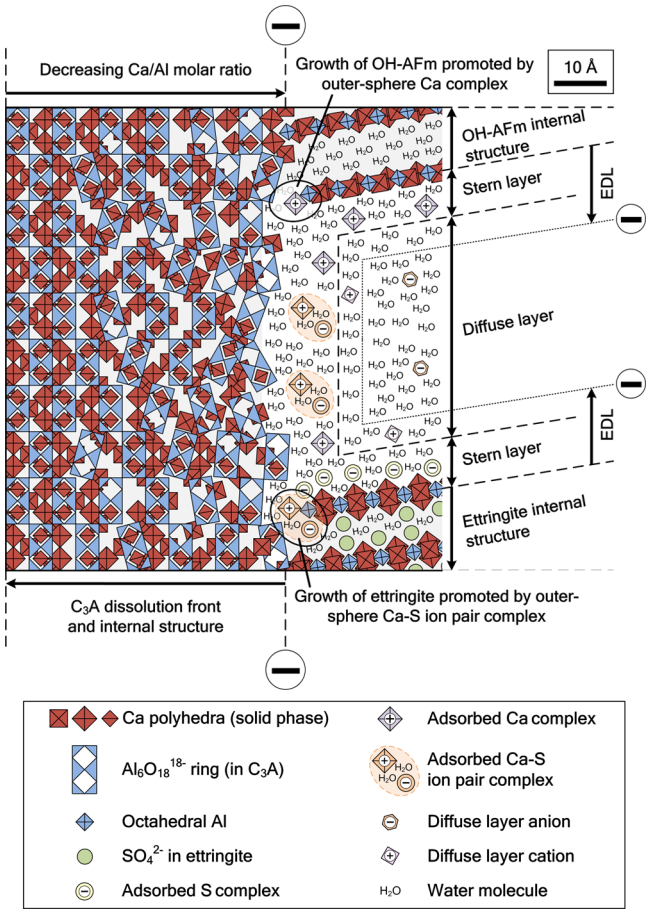

Figure 5. Schematic representation of the model C_3A/solution interface in aqueous $CaSO_4$ solution with initially formed AFm (e.g., at 80 s in 0.013 M $CaSO_4$, Figure 2F) and subsequently precipitated ettringite (e.g., during dissolution of C_3A in aqueous solution saturated with respect to $CaSO_4$ and $Ca(OH)_2$[6]) at pH >12, showing the outer-sphere adsorption of Ca and Ca−S ion pair complexes ($CaSO_4^0$) onto partially dissolved C_3A. AFm is depicted as OH-AFm without precluding the precipitation of AFm with other intercalated anions (e.g., SO_4^{2-}). The positions, number, and size of the model units shown are approximate: readers are referred to the crystallographic literature for accurate structures of the solid phases depicted.[4,5,52] C_3A dissolution is occurring from right to left and is shown to rearrange near-surface structural units in the Al-rich leached layer. The C_3A surface is depicted to bear a negative charge, which is expected at pH >12, from the preferential dissolution of Ca structural units[17] and from outer-sphere Ca adsorption in this pH range. The EDL and Stern layer are both enlarged relative to their expected size in fresh PC systems ($I \approx 0.4$ mol kg^{-1},[60] thus $\kappa^{-1} \approx 4$ Å in the absence of organic compounds).

DOI: 10.1021/acs.langmuir.6b03474
Langmuir 2017, 33, 45−55

and when the bulk aqueous S concentration approaches 0 in hydrated C_3A and gypsum[6]).

The adsorption of PNS onto C_3A, which is indicated by the zeta potential analysis shown in section 2.1 (Figure 2E), can be anticipated to further inhibit C_3A dissolution by blocking reactive surface sites. This interpretation is corroborated by isothermal calorimetry results.[13] The dissolution-inhibiting effect of PNS would be stronger if it is added initially to the aqueous solution prior to introducing C_3A rather than afterward because surface precipitates could partially hinder the transport of PNS to the C_3A surface (e.g., through adsorption). Additional evidence supporting the assignment of PNS adsorption to strongly inhibit C_3A dissolution is found in the similar inhibiting action of nitrile-tris(methylene)-phosphonic acid ($N[CH_2PO(OH)_2]_3$), which deprotonates at neutral to high pH, forms bidentate complexes with Ca, and grows to form stable precipitate $[N[CH_2PO(OH)_2]_2[CH_2PO(OOCa)](H_2O)]_n \cdot 3.5H_2O$.[19] This pairing to form $CH_2PO(OOCa)$ functional groups may analogously occur between PNS and Ca and potentially also between Ca−S complexes and the partially dissolved C_3A surface. This latter effect would enhance the nucleation and growth of surface-bound precipitates (e.g., ettringite, Figure 5) and inhibit C_3A dissolution if the blocking of reactive surface sites outweighs the relative increase in undersaturation that would occur through the removal of Ca and S from solution (e.g., when aqueous Ca and S concentrations are effectively constant before complete gypsum dissolution in the C_3A−gypsum−H_2O system[6]). The hydration of C_3A and PC is also inhibited by phosphates (e.g., Na_3PO_4[10,61]), which form strong ion pair complexes with both Ca (e.g., $CaHPO_4^0$) and Al (e.g., $AlH_2PO_4^{2+}$) and can further support the significant role of Ca−S complex adsorption in the model.

On the basis of the model proposed here (Figure 5), compounds that adsorb onto the Al-rich leached layer of partially dissolved C_3A and contain Ca (e.g., $CaSO_4^0$) and block reactive surface sites (e.g., PNS) are expected to inhibit C_3A dissolution. These types of compounds can also be expected to inhibit the dissolution of other phases with chemistry similar to that of C_3A (e.g., tetracalcium aluminoferrite), which is experimentally observed.[19] Therefore, the proposed C_3A dissolution model provides a more unified description of the rate-controlling factor in aqueous C_3A and $CaSO_4$ systems, and by extension PC systems, than previously reported. This understanding can be used to facilitate the development of improved chemical admixtures for fresh PC concrete to improve the workability of this material. However, further experimental and modeling work is needed to clarify the molecular structure of adsorbates in aqueous C_3A systems and the surface chemistry of partially dissolved C_3A. This article represents a preliminary step toward that goal.

4. CONCLUSIONS

This article presented experimental results on the chemistry and morphology of the C_3A/solution interface in aqueous Ca-, S-, and PNS-containing aqueous solutions and a model of C_3A dissolution that is consistent with the data presented and is relevant to fresh PC concrete. The zeta potential and pH results showed that the diffuse layer of C_3A is compressed as a function of increasing ionic strength, with SO_4^{2-} much more effectively compressing the diffuse layer than Cl^- irrespective of the balancing cation (K^+ or Ca^{2+}). These data also showed that the IEP of C_3A occurs at pH ∼12 and that there is an absence of EDL charge reversal caused by S or Ca. This latter result was interpreted to indicate that these elements do not alone provide the key C_3A dissolution rate controlling factor in fresh PC concrete. The SEM, X-ray ptychography, and S and Ca *K*-edge XAS data obtained were consistent with this interpretation. Together with existing data that show that C_3A dissolution in aqueous solution is greatly inhibited in the presence of Ca and S but not additional S alone, a model was proposed whereby the formation of an Al-rich leached layer and the adsorption of Ca−S ion pair complexes onto this leached layer provide the key C_3A dissolution rate limiting effect(s) in fresh PC concrete. This model also describes how macromolecules such as polyphosphonic acids and PNS are able to inhibit C_3A dissolution by blocking reactive surface sites through adsorption.

Morphological information on the C_3A/solution interface obtained by SEM and X-ray ptychography indicated that predominantly AFm phases, including S-AFm and consistent with the S and Ca *K*-edge XAS data, precipitated on the partially dissolved C_3A particles analyzed here. Low to moderate coverage of these phases on C_3A particles was found. Together with the zeta potential and pH data obtained, the results demonstrated that these surface precipitates partially contribute to but do not dominate the zeta potential results. Therefore, the proposed C_3A dissolution model reconciles the results obtained here and reported in the literature, advancing the understanding of C_3A dissolution in aqueous $CaSO_4$ solutions.

■ ASSOCIATED CONTENT

Supporting Information

The Supporting Information is available free of charge on the ACS Publications website at DOI: 10.1021/acs.langmuir.6b03474.

The procedures used to synthesize S- and OH-AFm are described in Appendix A. XRD, TGA, PSD, and specific surface area data of solid phases are shown in Appendix B. Plots of the pH >10 regions in Figure 1A−E are shown in Appendix C. Appendix D contains a reanalysis of the data presented in ref 40. (PDF)

■ AUTHOR INFORMATION

Corresponding Author

*E-mail: rupert.myers@gmail.com. Tel: +1 510 646 6106.

ORCID

Rupert J. Myers: 0000-0001-6097-2088

Notes

The authors declare no competing financial interest.

■ ACKNOWLEDGMENTS

The postdoctoral research of Rupert J. Myers at the University of California, Berkeley, was funded by Siam Cement Public Company (SCG) Ltd. Research done at the Advanced Light Source is supported by the Director, Office of Science, Office of Basic Energy Sciences of the U.S. Department of Energy under contract no. DE-AC02-05CH11231. This research was funded by the Republic of Singapore's National Research Foundation through a grant to the Berkeley Education Alliance for Research in Singapore (BEARS) for the Singapore-Berkeley Building Efficiency and Sustainability in the Tropics (SinBerBEST) Program. BEARS has been established by the University of

DOI: 10.1021/acs.langmuir.6b03474
Langmuir 2017, 33, 45−55

California, Berkeley as a center for intellectual excellence in research and education in Singapore. The study was also sponsored by the LNLS (Brazilian Synchrotron Light Laboratory) under project SXS1785/18902. The Laboratory of Ceramics (LACER, UFRGS) is thanked for the N_2 adsorption and particle size distribution results, and we thank Carlos A. O. Rios for insightful discussions on admixtures, Ubonwan Khopongpaiboon, Panod Viseschchitra, Thanakrit Chantra, and Anutchanan Kongkoon for help with S *K*-edge XAS (SLRI), David A. Shapiro for help with X-ray ptychography (ALS), Timothy Teague for support with XRD and XRF, Sunxiang Zheng for help with the electrophoresis experiments, and Lucas Girotto, Marlon Longhi, and Flavio C. Vicentin for the Ca *K*-edge XAS results (LNLS). Financial support from CNPq BJT grant 406684/2013-8 and CNPq PQ grant 309949/2014-9 is acknowledged.

REFERENCES

(1) van Oss, H. G. *Mineral commodity summaries*: cement.minerals.usgs.gov, accessed Dec 17, 2015.
(2) Taylor, H. F. W. *Cement Chemistry*, 2nd ed.; Thomas Telford Publishing: London, 1997.
(3) Nishi, F.; Takéuchi, Y. The Al_6O_{18} rings of tetrahedra in the structure of $Ca_{8.5}NaAl_6O_{18}$. *Acta Crystallogr., Sect. B: Struct. Crystallogr. Cryst. Chem.* **1975**, *B31*, 1169−1173.
(4) Mondal, P.; Jeffery, J. W. The crystal structure of tricalcium aluminate, $Ca_3Al_2O_6$. *Acta Crystallogr., Sect. B: Struct. Crystallogr. Cryst. Chem.* **1975**, *B31*, 689−697.
(5) Geng, G.; Myers, R. J.; Kilcoyne, A. L. D.; Ha, J.; Monteiro, P. J. M. Ca $L_{2,3}$-edge near edge X-ray absorption fine structure of tricalcium aluminate, gypsum and calcium (sulfo)aluminate hydrates. *Am. Mineral.* **2016**, accepted for publication.
(6) Minard, H.; Garrault, S.; Regnaud, L.; Nonat, A. Mechanisms and parameters controlling the tricalcium aluminate reactivity in the presence of gypsum. *Cem. Concr. Res.* **2007**, *37* (10), 1418−1426.
(7) Lothenbach, B.; Winnefeld, F. Thermodynamic modelling of the hydration of Portland cement. *Cem. Concr. Res.* **2006**, *36* (2), 209−226.
(8) Black, L.; Breen, C.; Yarwood, J.; Deng, C. S.; Phipps, J.; Maitland, G. Hydration of tricalcium aluminate (C_3A) in the presence and absence of gypsum-studied by Raman spectroscopy and X-ray diffraction. *J. Mater. Chem.* **2006**, *16* (13), 1263−1272.
(9) Traetteberg, A. U. D.; Grattan-Bellew, P. E. Hydration of 3CaO·Al_2O_3 and 3CaO·Al_2O_3 + gypsum with and without $CaCl_2$. *J. Am. Ceram. Soc.* **1975**, *58* (5−6), 221−227.
(10) Edmeades, R. M.; Hewlett, P. C. Cement admixtures. *Lea's Chemistry of Cement and Concrete*; Butterworth-Heinemann: Oxford, 1998; pp 841−905.
(11) Marchon, D.; Flatt, R. J. Impact of chemical admixtures on cement hydration. In *Science and Technology of Concrete Admixtures*; Aïtcin, P.-C., Flatt, R. J., Eds.; Elsevier: Cambridge, 2016.
(12) Bonen, D.; Sarkar, S. L. The superplasticizer adsorption capacity of cement pastes, pore solution composition, and parameters affecting flow loss. *Cem. Concr. Res.* **1995**, *25* (7), 1423−1434.
(13) Alonso, M. M.; Puertas, F. Adsorption of PCE and PNS superplasticisers on cubic and orthorhombic C_3A. Effect of sulfate. *Constr. Build. Mater.* **2015**, *78*, 324−332.
(14) Tadros, M. E.; Jackson, W. Y.; Skalny, J. A. N. Study of the dissolution and electrokinetic behavior of tricalcium aluminate. In *Hydrosols and Rheology*; Kerker, M., Ed.; Academic Press: London, 1976; pp 211−223.
(15) Zingg, A.; Winnefeld, F.; Holzer, L.; Pakusch, J.; Becker, S.; Gauckler, L. Adsorption of polyelectrolytes and its influence on the rheology, zeta potential, and microstructure of various cement and hydrate phases. *J. Colloid Interface Sci.* **2008**, *323* (2), 301−312.
(16) Feldman, R. F.; Ramachandran, V. S. The influence of $CaSO_4.2H_2O$ upon the hydration character of $3CaO.Al_2O_3$. *Mag. Concr. Res.* **1966**, *18* (57), 185−196.
(17) Skalny, J. A. N.; Tadros, M. E. Retardation of tricalcium aluminate hydration by sulfates. *J. Am. Ceram. Soc.* **1977**, *60* (3−4), 174−175.
(18) Jansen, D.; Goetz-Neunhoeffer, F.; Lothenbach, B.; Neubauer, J. The early hydration of ordinary Portland cement (OPC): an approach comparing measured heat flow with calculated heat flow from QXRD. *Cem. Concr. Res.* **2012**, *42* (1), 134−138.
(19) Bishop, M.; Bott, S. G.; Barron, A. R. A new mechanism for cement hydration inhibition: solid-state chemistry of calcium nitrilotris(methylene)triphosphonate. *Chem. Mater.* **2003**, *15* (16), 3074−3088.
(20) Scrivener, K. L.; Juilland, P.; Monteiro, P. J. M. Advances in understanding hydration of Portland cement. *Cem. Concr. Res.* **2015**, *78A*, 38−56.
(21) Bullard, J. W.; Jennings, H. M.; Livingston, R. A.; Nonat, A.; Scherer, G. W.; Schweitzer, J. S.; Scrivener, K. L.; Thomas, J. J. Mechanisms of cement hydration. *Cem. Concr. Res.* **2011**, *41* (12), 1208−1223.
(22) Sposito, G. *The Chemistry of Soils*, 2nd ed.; Oxford University Press: New York, 2008.
(23) Wijnja, H.; Schulthess, C. P. Vibrational spectroscopy study of selenate and sulfate adsorption mechanisms on Fe and Al (hydr)oxide surfaces. *J. Colloid Interface Sci.* **2000**, *229* (1), 286−297.
(24) Sigg, L.; Stumm, W. The interaction of anions and weak acids with the hydrous goethite (α-FeOOH) surface. *Colloids Surf.* **1981**, *2* (2), 101−117.
(25) Charlet, L.; Dise, N.; Stumm, W. Acidification of soil sulfate adsorption on a variable charge soil and on reference minerals. *Agric., Ecosyst. Environ.* **1993**, *47* (2), 87−102.
(26) Peak, D. Adsorption mechanisms of selenium oxyanions at the aluminum oxide/water interface. *J. Colloid Interface Sci.* **2006**, *303* (2), 337−345.
(27) Siretanu, I.; Ebeling, D.; Andersson, M. P.; Stipp, S. L. S.; Philipse, A.; Stuart, M. C.; van den Ende, D.; Mugele, F. Direct observation of ionic structure at solid-liquid interfaces: a deep look into the Stern Layer. *Sci. Rep.* **2014**, *4*, 4956.
(28) Huang, C.-P.; Stumm, W. Specific adsorption of cations on hydrous γ-Al_2O_3. *J. Colloid Interface Sci.* **1973**, *43* (2), 409−420.
(29) Sposito, G. The operational definition of the zero point of charge in soils. *Scol Sci. Soc. Am. J.* **1981**, *45* (2), 292−297.
(30) Stumm, W. Reactivity at the mineral-water interface: dissolution and inhibition. *Colloids Surf., A* **1997**, *120* (1−3), 143−166.
(31) Sposito, G. Gouy-Chapman Theory. In *Encyclopedia of Geochemistry*; White, W. M., Ed.; Encyclopedia of Earth Sciences Series; Springer: New York, 2016.
(32) Yoshioka, K.; Tazawa, E.-I.; Kawai, K.; Enohata, T. Adsorption characteristics of superplasticizers on cement component minerals. *Cem. Concr. Res.* **2002**, *32* (10), 1507−1513.
(33) Plank, J.; Hirsch, C. Impact of zeta potential of early cement hydration phases on superplasticizer adsorption. *Cem. Concr. Res.* **2007**, *37* (4), 537−542.
(34) Medala, M.; Labbez, C.; Pochard, I.; Nonat, A. Ettringite surface chemistry: interplay of electrostatic and ion specificity. *J. Colloid Interface Sci.* **2011**, *354* (2), 765−770.
(35) Elakneswaran, Y.; Nawa, T.; Kurumisawa, K. Electrokinetic potential of hydrated cement in relation to adsorption of chlorides. *Cem. Concr. Res.* **2009**, *39* (4), 340−344.
(36) Shapiro, D. A.; Yu, Y.-S.; Tyliszczak, T.; Cabana, J.; Celestre, R.; Chao, W.; Kaznatcheev, K.; Kilcoyne, A. L. D.; Maia, F.; Marchesini, S.; Meng, Y. S.; Warwick, T.; Yang, L. L.; Padmore, H. A. Chemical composition mapping with nanometre resolution by soft X-ray microscopy. *Nat. Photonics* **2014**, *8* (10), 765−769.
(37) Hunter, R. J. *Zeta Potential in Colloid Science: Principles and Applications*, 3rd ed.; Academic Press: London, 1988.
(38) Stumm, W. Aquatic colloids as chemical reactants: surface structure and reactivity. *Colloids Surf., A* **1993**, *73*, 1−18.

DOI: 10.1021/acs.langmuir.6b03474
Langmuir 2017, 33, 45−55

(39) Ravel, B.; Newville, M. ATHENA, ARTEMIS, HEPHAESTUS: data analysis for X-ray absorption spectroscopy using IFEFFIT. *J. Synchrotron Radiat.* **2005**, *12*, 537−541.
(40) Collepardi, M.; Baldini, G.; Pauri, M.; Corradi, M. Tricalcium aluminate hydration in the presence of lime, gypsum or sodium sulfate. *Cem. Concr. Res.* **1978**, *8* (5), 571−580.
(41) Tenoutasse, N. The hydration mechanism of C_3A and C_3S in the presence of calcium chloride and calcium sulfate. *Proceedings of the Fifth International Symposium on the Chemistry of Cement (II)*; Tokyo, 1968.
(42) Bourg, I. C.; Sposito, G. Molecular dynamics simulations of the electrical double layer on smectite surfaces contacting concentrated mixed electrolyte (NaCl−$CaCl_2$) solutions. *J. Colloid Interface Sci.* **2011**, *360* (2), 701−715.
(43) Lasaga, A. C.; Lüttge, A. Mineralogical approaches to fundamental crystal dissolution kinetics. *Am. Mineral.* **2004**, *89* (4), 527−540.
(44) Chrysochoou, M.; Dermatas, D. Evaluation of ettringite and hydrocalumite formation for heavy metal immobilization: literature review and experimental study. *J. Hazard. Mater.* **2006**, *136* (1), 20−33.
(45) Myers, D. *Surfactant Science and Technology*; John Wiley & Sons: Hoboken, NJ, 2006.
(46) Hekal, E. E.; Kishar, E. A. Effect of sodium salt of naphthalene-formaldehyde polycondensate on ettringite formation. *Cem. Concr. Res.* **1999**, *29* (10), 1535−1540.
(47) Pourchet, S.; Regnaud, L.; Perez, J. P.; Nonat, A. Early C_3A hydration in the presence of different kinds of calcium sulfate. *Cem. Concr. Res.* **2009**, *39* (11), 989−996.
(48) Fleet, M. E.; Liu, X.; Harmer, S. L.; King, P. L. Sulfur *K*-edge XANES spectroscopy: chemical state and content of sulfur in silicate glasses. *Can. Mineral.* **2005**, *43*, 1605−1618.
(49) Wieland, E.; Dähn, R.; Vespa, M.; Lothenbach, B. Micro-spectroscopic investigation of Al and S speciation in hardened cement paste. *Cem. Concr. Res.* **2010**, *40* (6), 885−891.
(50) Vespa, M.; Wieland, E.; Dähn, R.; Grolimund, D.; Scheidegger, A. M. Determination of the elemental distribution and chemical speciation in highly heterogeneous cementitious materials using synchrotron-based micro-spectroscopic techniques. *Cem. Concr. Res.* **2007**, *37* (11), 1473−1482.
(51) Mishra, A.; Parsai, N.; Shrivastava, B. D. Simplified analysis of EXAFS data and determination of bond lengths. *Indian J. Pure Appl. Phys.* **2011**, *49*, 25−29.
(52) Moore, A. E.; Taylor, H. F. W. Crystal structure of ettringite. *Acta Crystallogr., Sect. B: Struct. Crystallogr. Cryst. Chem.* **1970**, *B26*, 386−393.
(53) Allmann, R. Refinement of the hybrid layer structure $[Ca_2Al(OH)_6]^+[1/2SO_4{\cdot}3H_2O]^-$. *Neues Jahrb. Mineral. Monatsh.* **1977**, *3*, 136−144.
(54) Pedersen, B. F.; Semmingsen, D. Neutron diffraction refinement of the structure of gypsum, $CaSO_4{\cdot}2H_2O$. *Acta Crystallogr., Sect. B: Struct. Crystallogr. Cryst. Chem.* **1982**, *B38*, 1074−1077.
(55) Okoronkwo, M. U.; Glasser, F. P. Compatibility of hydrogarnet, $Ca_3Al_2(SiO_4)_x(OH)_{4(3-x)}$, with sulfate and carbonate-bearing cement phases: 5−85 °C. *Cem. Concr. Res.* **2016**, *83*, 86−96.
(56) Eichert, D.; Salomé, M.; Banu, M.; Susini, J.; Rey, C. Preliminary characterization of calcium chemical environment in apatitic and non-apatitic calcium phosphates of biological interest by X-ray absorption spectroscopy. *Spectrochim. Acta, Part B* **2005**, *60* (6), 850−858.
(57) Sowrey, F. E.; Skipper, L. J.; Pickup, D. M.; Drake, K. O.; Lin, Z.; Smith, M. E.; Newport, R. J. Systematic empirical analysis of calcium-oxygen coordination environment by calcium *K*-edge XANES. *Phys. Chem. Chem. Phys.* **2004**, *6* (1), 188−192.
(58) Pattanaik, S.; Huffman, G. P.; Sahu, S.; Lee, R. J. X-ray absorption fine structure spectroscopy and X-ray diffraction study of cementitious materials derived from coal combustion by-products. *Cem. Concr. Res.* **2004**, *34* (7), 1243−1249.
(59) Glasser, F. P.; Marinho, M. B. Early stages of the hydration of calcium aluminate and its sodium-containing solid solutions. *Br. Ceram. Soc. J.* **1984**, *35*, 222−236.
(60) Rothstein, D.; Thomas, J. J.; Christensen, B. J.; Jennings, H. M. Solubility behavior of Ca-, S-, Al-, and Si-bearing solid phases in Portland cement pore solutions as a function of hydration time. *Cem. Concr. Res.* **2002**, *32* (10), 1663−1671.
(61) Lieber, V. W. Effect of inorganic admixtures on the setting and hardening of Portland cement. *Zem.-Kalk-Gips* **1973**, *26*, 75−79.

DOI: 10.1021/acs.langmuir.6b03474
Langmuir 2017, 33, 45−55